Nanoscale

PAPER

View Article Online
View Journal | View Issue

Cite this: *Nanoscale*, 2025, **17**, 12797

The impact of ferrocenium as a catalyst on the chiral distribution of single-walled carbon nanotubes in floating-catalyst chemical vapor deposition synthesis†

Anastasios Karakassides, *[a] Hirotaka Inoue,[a,b] Peng Liu, [a] Zhenyu Xu, [a] Ghulam Yasin,[a] Hua Jiang[a] and Esko I. Kauppinen*[a]

Received 21st January 2025,
Accepted 21st April 2025

DOI: 10.1039/d5nr00297d

rsc.li/nanoscale

In response to the growing demand for novel catalyst designs for the selective growth of single-walled carbon nanotubes (SWCNTs), this study explores the use of ferrocenium (the oxidized state of ferrocene) as a new catalyst precursor for the first time. Utilizing the floating-catalyst chemical vapor deposition (FC-CVD) method, SWCNTs were synthesized and characterized through analytical transmission electron microscopy selected area electron diffraction (TEM SAED) and optical techniques (Raman spectroscopy and UV-vis-NIR absorption). The introduction of ferrocenium led to an enhancement in the metallicity of the nanotubes, increasing the proportion of metallic SWCNTs to 43.1%, while also broadening the nanotube mean diameter from 1.84 nm to 2.10 nm. The key factor behind this improvement lies in the positive charge of Fe^{3+} in ferrocenium, which has been shown to stabilize metallic nanotube formation. These findings highlight the pivotal role of catalyst charge in controlling SWCNT chirality and electronic properties, paving the way for more precise control in nanotube synthesis for applications in nanoelectronics and materials science.

1. Introduction

Single-walled carbon nanotubes (SWCNTs) possess a remarkable blend of properties (large surface area, electrical conductivity, and mechanical strength) and tunable characteristics that make them excellent candidate materials for a wide range of applications, ranging from flexible displays[1] and use in electrochemical energy conversion to storage procedures[2], to biomedical engineering applications such as drug delivery,[3,4] and environmental remediation for pollutant removal.[5,6] One of the biggest challenges to nanotube synthesis currently is the selective growth of structurally uniform SWCNTs *via* chemical vapor deposition (CVD) under high yield conditions that can allow easier industrialization of these materials.

Chirality is a critical factor in determining the properties of SWCNTs because it directly influences whether they behave as semiconductors (s-SWCNTs) or metals (m-SWCNTs), affecting their potential applications.[7] About two-thirds of SWCNTs with specific chiralities exhibit semiconducting behavior, making them ideal for use in transistors,[8] solar cells,[9] and flexible electronics,[10] while one-third behaves like metals, suitable for applications such as interconnects in circuits[11] and conductive composites.[12] In addition to electronic properties, chirality also affects the mechanical strength of SWCNTs[13] and their growth rate during synthesis.[14] Given the significant impact chirality has on both the functional properties and production efficiency of SWCNTs, controlling it during synthesis is crucial. Achieving selective control of chirality would enable the tailored design of SWCNTs for specific applications, unlocking their full potential in fields such as electronics, energy storage, and materials engineering.

Lately, one promising route for selective chirality during synthesis that has gained attention is the engineering of novel catalysts that possess a specific structure. Traditionally, these catalysts have comprised combinations of two low-melting temperature transition metals (such as Fe, Ni, or Co), but recent developments have explored the utilization of one high-melting temperature metal (or non-metal) such as Re,[15] Rh,[16] W,[17,18] WC,[19] and Mo_2C[20] alongside a low-melting one or even alone. Depending on the metals selected, the pursuit of

---

[a] *Department of Applied Physics, School of Science, Aalto University, Puumiehenkuja 2, 02150 Espoo, Finland. E-mail: anastasios.karakasidis@aalto.fi, esko.kauppinen@aalto.fi*

[b] *Sumitomo Electric Industries, Ltd, 1-1-3 Shimaya, Konohana-ku, Osaka 554-0024, Japan*

† Electronic supplementary information (ESI) available. See DOI: **https://doi.org/10.1039/d5nr00297d**

bimetallic catalyst combinations involves modifying the morphology and composition of the catalyst and its final melting temperature. This change in melting point may therefore have an impact on the cap formation and carbon incorporation at the open ends of SWCNTs as a result of the different physical states of the metals of the catalyst. These differences in the early formation of carbon rings are closely related to the surface structure of the catalyst, demonstrating a "template effect" marked by a predominance of hollow site occupancy.[21]

More specifically, Feng Zhang *et al.*[22] managed to synthesize SWCNTs with a narrow-diameter distribution of about 1.35 nm by utilizing a bi-metallic CoRu catalyst supported on an SiO_2 substrate. Their results revealed an enrichment of armchair nanotubes by almost 12%, based mostly on Raman spectroscopy characterization. Xin Li *et al.*[15] synthesized m-SWCNTs with an abundance of 80% using a $CoRe_4$ catalyst possessing a hexagonal close-packed structure. According to the authors, the result of their synthesis was achieved because of the lower binding energy between their catalyst and the m-SWCNTs, which promoted their growth rate. Similarly, W_6Co_7 alloy nanoparticles have shown promising results on selective chiral growth of SWCNTs, where Feng Yang *et al.*[23] reported an abundance of 94.4% (12,6) nanotubes based on Raman and optical spectroscopy methods. According to these authors, by utilizing functional theory simulations, their alloy nanoparticles possessed the perfect geometrical match for (12,6) nanotubes while exhibiting extremely low matches for all other chiralities. These advancements in catalyst design and synthesis methods have paved the way for further exploration of various strategies aimed at achieving selective growth of SWCNTs, such as the introduction of etchants during the synthesis process, commonly referred to as selective etching.

During the last few years, various efforts have been made to achieve the desired selective growth of SWCNTs, including introduction of etchants during the synthesis[24–30] (known as selective etching). Selective etching involves the introduction of an oxidizing environment during the synthesis process (methanol, water vapor, oxygen, combinations of H_2O and CO_2, *etc.*), in which it is possible to etch smaller diameter reactive m-SWCNTs.[31] Moreover, it has been shown that H_2O vapor in specific amounts could significantly affect the nucleation of s-SWCNTs, while it should be noted that many gaseous by-products of the decomposition of various alcohols (ethanol and IPA) could include H_2O and/or CO_2 that contribute to this etching as well.[32] Apart from the efforts to selectively etch m-SWCNTs, significant attention has also been given to etch s-SWCNTs. For instance, Yongping Liao *et al.*[33] have grown SWCNT films with a metal/semiconductor ratio of 46.3% by introducing various amounts of CO_2 into floating-catalyst CVD (FC-CVD) using CO as a carbon source. They suggested that CO_2 could affect the CO disproportionation and nucleation modes of SWCNTs, resulting in various diameter ranges of the SWCNTs. Moreover, Qiangmin Yu *et al.*[34] explored the enrichment of m-SWCNTs using NO_2 to selectively etch s-SWCNTs, achieving purity values higher than 90%. Besides selective etching, recent studies have also emphasized controlling chirality by focusing on the chemical state of catalyst precursors.

One recent research study by Sook Young Moon *et al.*[35] explored the effect of oxygen-containing functional groups in ferrocene ($FeCp_2$)-derived catalyst precursors. They utilized ferrocenemethanol (–OH functional group), acetylferrocene (C=O functional group), and 1,1′-diacetylferrocene (C=O functional group) to investigate their influence on the synthesis of SWCNTs. According to these authors, the pyrolysis and release of Fe ions were delayed by the functional groups of the ferrocene-derived precursors compared to ferrocene alone, leading to variations in SWCNT growth. The variations in SWCNT growth caused by the delayed release of Fe ions from ferrocene-derived precursors highlight the importance of accurately assessing the chirality of the resulting nanotubes. Given the sensitivity of CNT growth based on catalyst precursor chemistry, more efforts need to be made to investigate the effect of this complex chemistry on the structure of synthesized nanotubes (chirality, diameter, crystallinity *etc.*).

In this context, we considered ferrocenium, the oxidized form of ferrocene, an iron precursor frequently used in FC-CVD, to be a worthy material for investigation. It has been widely employed in various fields due to its unique redox properties, stability, and ability to act as an electron-transfer mediator.[36] It has found applications in areas such as electrochemical sensors[37] and materials science,[38] particularly as a redox catalyst in polymerization reactions.[39,40] These applications leverage ferrocenium's ability to facilitate electron transfer and its compatibility with a range of chemical environments. Despite its versatile use in other domains, ferrocenium has never been explored as a catalyst for single-walled carbon nanotube (SWCNT) synthesis. This gap is particularly intriguing given the critical need for selective growth of metallic SWCNTs (m-SWCNTs) with high yield and precision.

In particular, the evaluation of chirality is quite challenging and more attention needs to be given to the reliability of reported results that have not coupled all of the available techniques (*e.g.* TEM SAED, Raman spectroscopy, and UV-vis-NIR spectroscopy). It is crucial to pay careful attention to the accuracy of these chirality evaluation techniques, as they directly impact the interpretation of growth outcomes. Raman spectroscopy, one of the most widely used methods for evaluating chirality, has been employed in many studies as mentioned before, which reported high yields of m-SWCNTs.[19,41] However, some reports suggest that Raman spectroscopy may have low reliability for quantitative evaluation of chirality[42] and diameter.[43]

Motivated by these different results and addressing the pressing challenges in catalyst design, we investigated ferrocenium for the first time as a novel catalyst to enrich m-SWCNT growth. By utilizing the FC-CVD method, SWCNTs were grown in high yields and the nature of the nanotubes was assessed through analytical TEM SAED studies supported by optical characterization techniques (Raman spectroscopy and UV-vis-NIR light absorption).

2. Materials and methods

2.1 SWCNT synthesis

High-quality pure anhydrous ethanol (ETAX Aa, 99.5%, Anora, Finland) was used as the carbon source, while ferrocene (99%, Alfa Aesar) and thiophene (≥99%, Sigma-Aldrich) were utilized as the catalyst and promoter precursors, respectively. For the oxidation of ferrocene to ferrocenium, copper(ɪɪ) nitrate trihydrate puriss. p.a., 99–104% (Sigma-Aldrich), was utilized. An ethanol solution containing 0.5 wt% ferrocene, thiophene (atomic ratio of S/Fe ~ 0.3) and copper(ɪɪ) nitrate (atomic ratio of Cu/Fe from 0.3 to 0.5) was sonicated for 2 min in a vial to form a homogeneous solution and subsequently injected into a heating line at 250 °C (enabled by a heating cord and a benchtop thermocouple controller from BriskHeat, USA) using a syringe pump (NE-1000 series, New Era Pump Systems, USA) operating at a constant feed rate of 6 $\mu L\ min^{-1}$. The evaporated precursors were carried into the reactor's heating zone using 1000 standard cubic centimeters (sccm) of N_2 (AGA, Finland, filtered through an oxygen/moisture purifier, OT3-4, Agilent) and 400 sccm of H_2 (99.999%, AGA, Finland). The reactor temperature for SWCNT synthesis was set at 1040 °C. The as-synthesized SWCNT film was collected at the outlet of the reactor (under ambient conditions) using an MF-Millipore membrane filter (Φ = 25 mm and a thickness of 150 µm, Merck Millipore) with a pore size of 0.45 µm.

2.2 UV-vis-NIR and Raman spectroscopy characterization

The SWCNT film was transferred initially to a glass slide using a straightforward press-transfer method and consequently analyzed using a UV-vis-NIR spectrometer (Agilent Cary 5000, Agilent Technologies, Inc., USA). The optical absorption spectra were normalized to the intensity of the π plasmon peak for each sample, while a MATLAB code was used to estimate the diameter distribution of the SWCNTs.[44] The metal to semiconductor ratio and yield of SWCNTs were calculated using analytical methods described in our previous studies.[45] A Horiba Jobin–Yvon Labram HR 800 Raman spectrometer (Horiba Ltd, Japan), offering four different excitation wavelengths (488 nm, 514 nm, 633 nm, and 785 nm), was used to obtain Raman spectra. To ensure consistency, the Raman spectra were normalized to the intensity of the graphitic (G) band.

2.3 Transmission electron microscopy, scanning electron microscopy and X-ray photoelectron spectroscopy characterization

For transmission electron microscopy (TEM) analysis, the SWCNTs were directly collected on a lacey carbon-coated Au TEM grid (300 mesh). A JEOL 2200FS double Cs-corrected TEM (JEOL Ltd, Japan) instrument was utilized for high-resolution imaging at 200 kV, while for the SAED patterns of the individual SWCNTs, an acceleration voltage of 80 kV was used. A Kratos AXIS-ULTRA X-ray photoelectron spectroscopy (XPS) system (SHIMADZU, Japan) was used for the elemental analysis of the synthesized samples. Energy dispersive spectroscopy (EDS) mapping of the fabricated SWCNTs was performed using a Zeiss Sigma VP scanning electron microscope (SEM) equipped with a Schottky field emission gun (FEG). SEM was performed at an acceleration voltage of 1.5 kV.

2.4 Measurement of the resistance of SWCNT thin films

The details of the four-point probe method used for measuring sheet resistance have been comprehensively covered in other studies.[45] It should be noted that each data point of the sheet resistance represents the average of three measurements taken from different locations on the SWCNT film and the measurements were made after washing/densification with isopropyl alcohol.

2.5 Aerosol net charge measurement

An aerosol electrometer 3068B (TSI Incorporated, USA) was utilized to measure the total net charge on aerosol particles from the reactor exhaust, providing real-time readings with a sensitivity of better than ±1 femtoampere (fA) RMS with a one-second averaging time. It was temperature stabilized to significantly reduce drift.

2.6 Evaluation of solution properties

Both UV-vis-NIR spectroscopy and pH measurements over time were employed to analyze the solution properties. Initially, the pH of the prepared solutions was measured (Mettler Toledo SevenCompact™ pH meter S210, Mettler Toledo, USA) and then the same solutions were analyzed using a UV-vis-NIR spectrometer as described before.

3. Results and discussion

3.1 Partial oxidation of ferrocene using copper(ɪɪ) nitrate trihydrate

The oxidation occurred in a solution containing ethanol, ferrocene ($FeCp_2$), thiophene, and copper(ɪɪ) nitrate trihydrate. Two solutions with different Cu/Fe atomic ratios were prepared, one with Cu/Fe of 0.3 and the other with Cu/Fe of 0.5. After mixing all the precursors, the solution was sonicated for 2 minutes to achieve homogeneity (Fig. 1a). Initially, the solution exhibited the characteristic yellow/orange colour of ferrocene in ethanol (Fig. 1b); however, over time, the colour gradually changed to green, starting as a light green (Fig. 1c) and eventually becoming a much darker green (Fig. 1d). This colour change indicates the partial oxidation of ferrocene, from the moment ferrocene is known for its yellow/orange colour, while its oxidized form, ferrocenium, has a deep blue colour.[46] The observed green colour results from the mixing of these two colours, with the intensity of the green colour deepening as the oxidation of ferrocene progresses. The colour of the solution changes over almost 24 hours until saturation is observed. It should be noted here that the plain ethanol–ferrocene–thiophene solution did not exhibit any colour change (yellowish colour) and the pH did not show any drop over time (Fig. 1e).

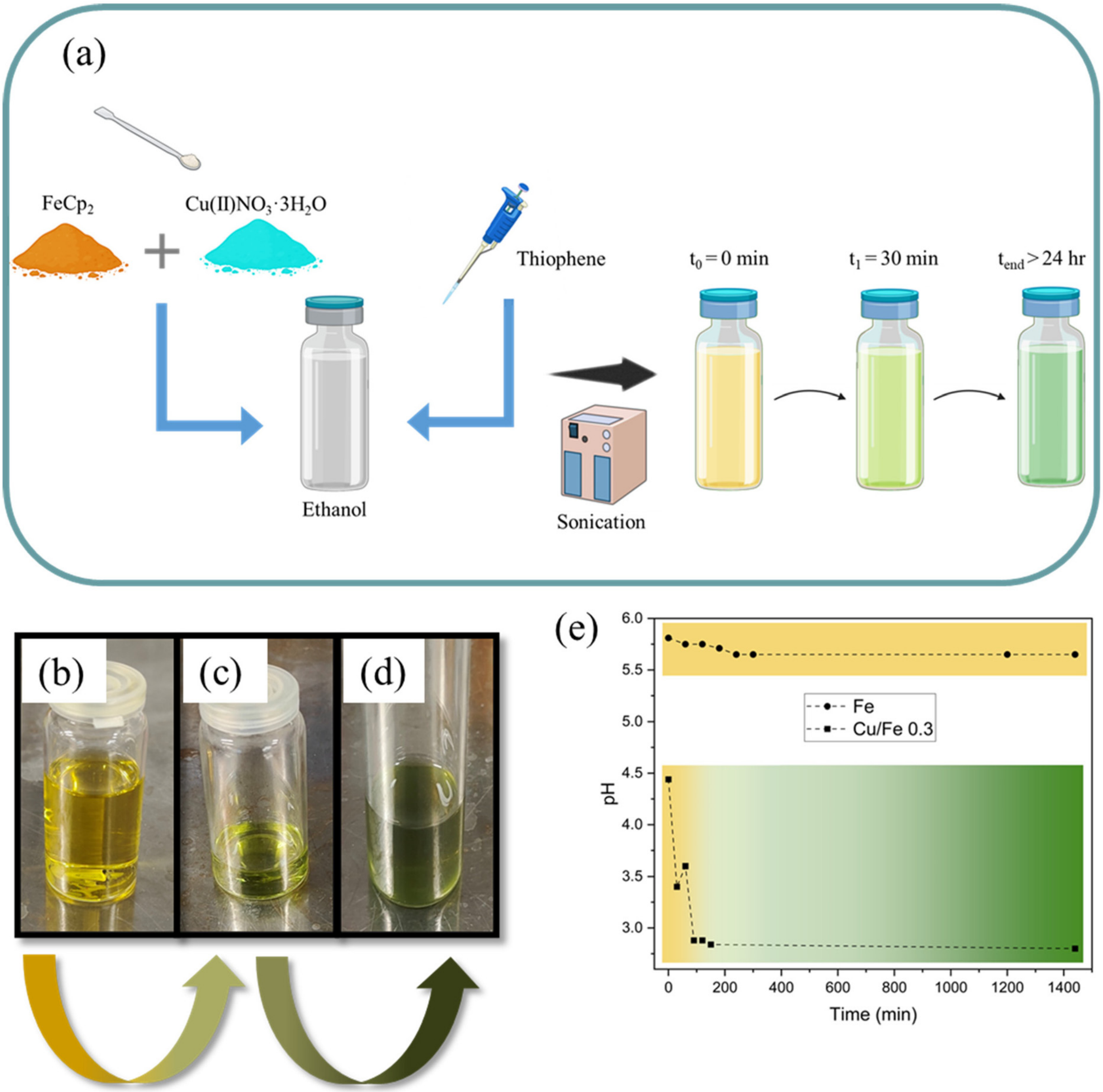

Fig. 1 Evolution of the Cu/Fe solution due to ferrocene oxidation over time. (a) Schematic of the solution preparation method. (b) Initial colour of the solution containing copper(II) nitrate trihydrate observed within 0–10 minutes. (c) Colour of the same solution after 30 minutes. (d) Colour of the same solution after 24 hours. (e) The evolution of pH over time for solutions with and without the ferrocene oxidation effect. In panel (e), the black circles represent the plain ethanol–ferrocene–thiophene solution, while the black squares correspond to the Cu/Fe 0.3 solution. Panels (b), (c), and (e) refer specifically to the oxidized ferrocene solution.

The mechanism of ferrocene oxidation can be found in the literature in acetonitrile instead of ethanol and is described by the following:

$$\mathrm{Cu^{II}(NO_3)_2 + FeCp_2 \rightarrow Cu^{I}(NO_3)_2 + FeCp_2{}^{+}} \qquad (1)$$

According to the literature,[47] the nitrate ion in this reaction mildly slows down the oxidation process, which is in good agreement with our results in that from the moment the oxidation begins it progresses slowly over time for more than 24 h, as previously mentioned. To monitor the oxidation reaction of ferrocene, both UV-vis-NIR spectroscopy and pH measurements over time were employed. Initially, the pH values of the prepared solutions were measured and then the same solutions were analysed using a light absorption spectrometer. From Fig. 1e, it can be seen that the pH was not stable but rather changes over time, revealing the progress of the oxidation reaction. Moreover, the pH value of a normal ferrocene–ethanol–thiophene solution was measured as well at 6.6, just for comparison purposes. The initial solution of yellowish colour exhibited a pH value of about 4.4 and after 24 h this value gradually decreased to 2.8, where saturation was observed. This was a clear indication that the oxidation reaction occurs slowly over 24 h in this solution. However, more analytical experiments were needed to justify the pH results.

For this reason, UV-vis-NIR spectroscopy was employed. The solution with Cu/Fe of 0.3 atomic ratio was analysed using the spectrometer during oxidation at 3 different stages: (i) the initial solution just after mixing all precursors (yellowish phase); (ii) after 30 min of rest (light green phase); and (iii) after 24 h of rest (dark green phase). Fig. 2a shows the light absorption results of all the samples. As can be seen from the spectra, the band at around 435 nm can be assigned to the characteristic ferrocene signal in ethanol solution, while the bands at 620 nm and 760 nm are assigned to ferrocenium[48] and copper(II) nitrate, respectively.[49] All the remaining bands can be attributed to the ethanol solution. During the oxidation of ferrocene, the intensity and area of the ferrocene band decreased (Fig. 2b), while that of the ferrocenium band increased, illustrating the progression of the oxidation process over time. By measuring and comparing the areas of these two characteristic bands (Fig. S1†), it is possible to determine the oxidation ratio (%) of the solution over time as follows:

$$\text{Oxidation ratio}\,(\%) = \frac{\text{area}_{\text{ferrocenium}}}{\text{area}_{\text{ferrocene}}} \times 100 \qquad (2)$$

Using eqn (2), the Cu/Fe 0.3 sample exhibited a maximum oxidation value of approximately 35% during 48 hours of testing. Initially, data points were collected every 10 minutes and after the first hour, data were recorded every hour (Fig. 2c). In contrast, the Cu/Fe 0.5 sample reached an oxidation value of nearly 47% over the same time frame, which was expected due to the higher copper content in this second sample, contributing to the increased levels of oxidized ferrocene over the same period.

3.2 Synthesis and characterization of SWCNTs

After assessing the solution properties as discussed earlier, the solution was fed into an FC-CVD reactor to grow SWCNTs and investigate the impact of the ferrocenium/ferrocene catalyst on

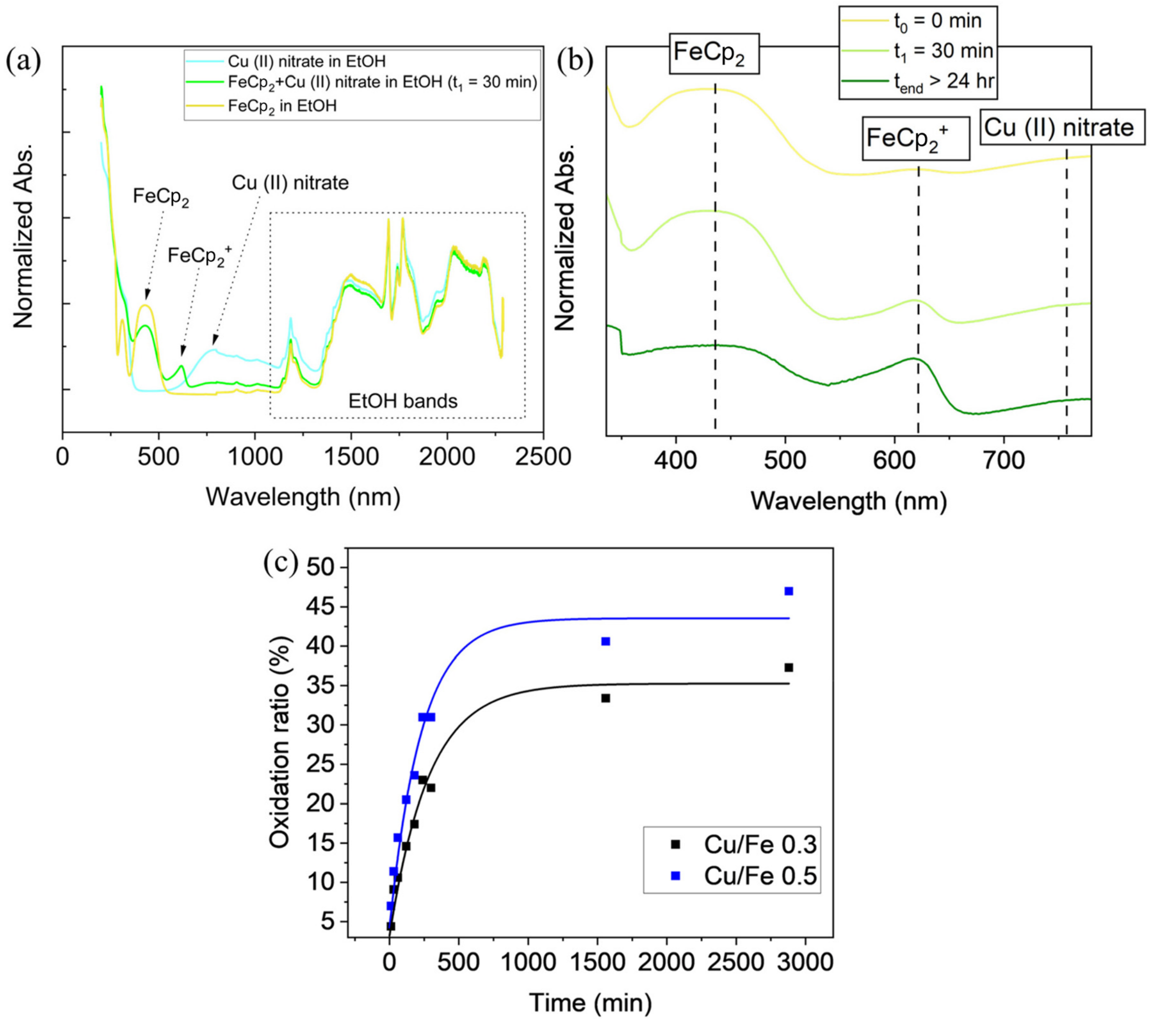

Fig. 2 (a) UV-vis-NIR absorption spectra of all samples, (b) UV-vis-NIR spectra of all samples during the oxidation process, and (c) oxidation ratio (%) of all samples over time.

the synthesis of nanotubes. The conditions of the reactor were kept the same for the ferrocene only and ferrocenium/ferrocene catalysts to ensure standard comparison between the samples. The macroscopic properties of SWCNTs were initially evaluated using Raman spectroscopy to examine if the samples were SWCNTs through the detection of breathing modes (RBM). The results are shown in Fig. S2.† Four different laser sources were used for these measurements (488 nm, 514 nm, 633 nm and 785 nm) and it can be confirmed that the samples were SWCNTs. However, the assignment of the chirality distribution was quite challenging with only four laser sources due to intertube coupling and the dominant brightness of certain chiral nanotubes in the Raman spectrum, and hence, other techniques were used, such as UV-vis-NIR spectroscopy and TEM SAED, for a more complete evaluation.

The first and second interband transitions of semiconducting nanotubes (S_{11} and S_{22}) and the first interband transition of metallic nanotubes (M_{11}) in the optical absorption spectra are the characteristic features that differentiate SWCNTs from other nanotube assemblies.[50–52] The wavelength range of these specific bands was used to estimate the diameters of SWCNTs, where S_{11} (~2100–2500 nm), S_{22} (~1200–1400 nm) and M_{11} (~800 nm) peaks are clearly visible in the absorption spectra, as shown in Fig. 3a. A redshift of the peak position of the bands can be observed with the addition of copper(II) nitrate trihydrate to the solution of precursors, indicating an increased mean diameter of SWCNTs. To estimate this increased mean diameter, the data were analysed utilizing a MATLAB code developed by Tian *et al.*[44] The SWCNTs grown from ferrocene only exhibited a mean diameter of about 1.84 nm, while Cu/Fe 0.3 and Cu/Fe 0.5 showed mean diameters of 2.10 nm and 2.09 nm, respectively (Fig. 3b–d).

To further investigate the light absorption spectra, TEM was employed (Fig. 4a–c). Samples were directly collected on TEM grids placed on the membrane in the collection filter area. To ensure that the sample's density did not impede electron transmission, a short collection time of 6–7 seconds was chosen. Subsequently, the samples were analysed using a 200 kV acceleration voltage in the microscope to obtain high-resolution micrographs. From the analysis of the micrographs, it can be seen that the Fe sample exhibited the smallest mean bundle diameter of 11.20 nm, while the Cu/Fe 0.3 and Cu/Fe

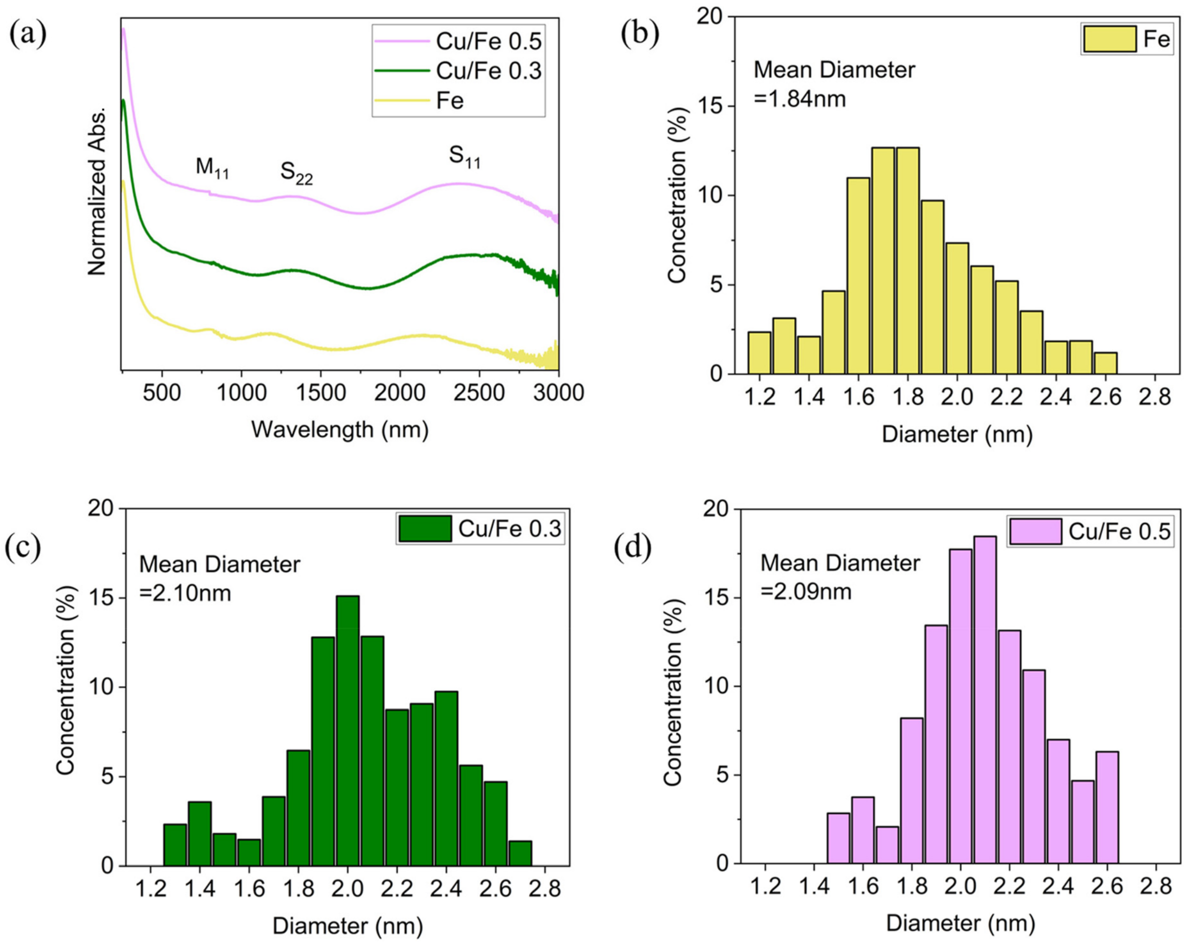

Fig. 3 UV-vis-NIR assessment of all samples. (a) Light absorption spectra, (b) diameter distribution of the Fe sample, (c) diameter distribution of the Cu/Fe 0.3 sample and (d) diameter distribution of the Cu/Fe 0.5 sample. The diameter distributions in this figure were plotted using a MATLAB code.

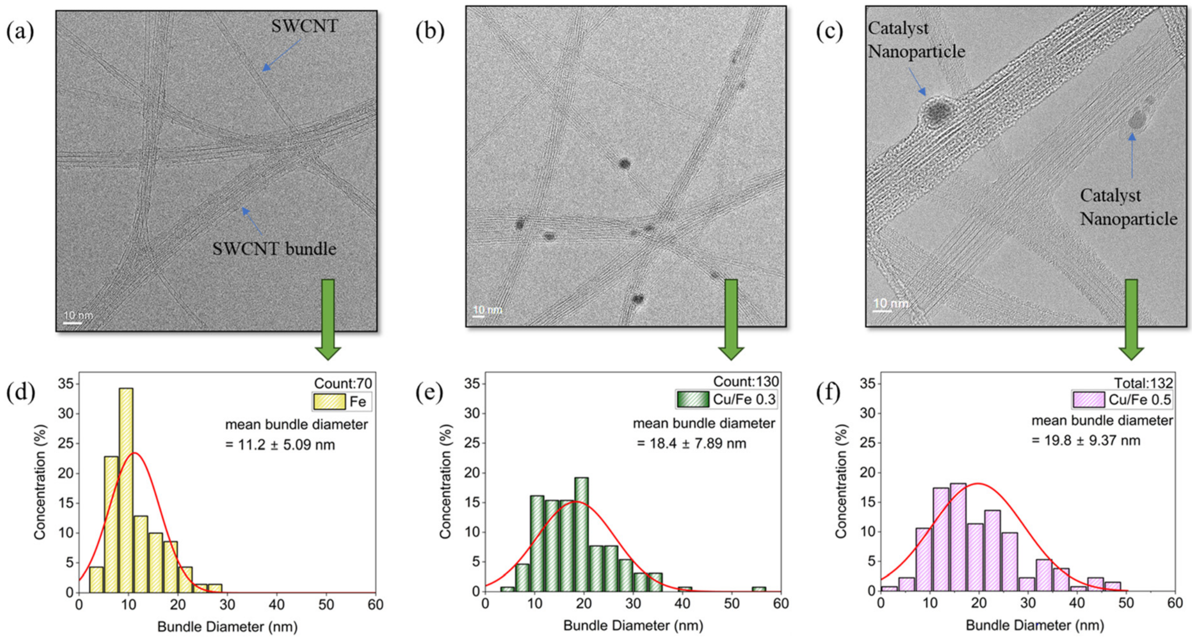

Fig. 4 TEM morphology characterization of the SWCNTs. (a) TEM micrograph of the Fe sample, (b) TEM micrograph of the Cu/Fe 0.3 sample, (c) TEM micrograph of the Cu/Fe 0.5 sample, (d) bundle diameter distribution of the Fe sample, (e) bundle diameter distribution of the Cu/Fe 0.3 sample, and (f) bundle diameter distribution of the Cu/Fe 0.5 sample.

0.5 samples exhibited mean diameters of 18.40 nm and 19.80 nm, respectively (Fig. 4d–f). There is an obvious increase (almost double in the case of Cu/Fe 0.5) in the mean bundle diameter with the introduction of copper(II) nitrate trihydrate into the synthesis process.

This bundle increment did not translate into much worse resistance values of the thin films, as can be seen in Fig. S3a.† It was expected that the samples with larger bundle diameter should exhibit decreased resistance values. It is well proven that reducing the concentration of CNTs during the FC-CVD process can lead to the formation of thinner SWCNT bundles, which is one of the most effective strategies for enhancing the conductivity of SWCNT films.[53,54] Apart from this, larger bundles tend to absorb more light because they have a higher density of nanotubes, providing more material to interact with the light, which leads to worse resistance values in the thin films from the moment the transmittance of the films is used for normalization of the resistance values. It should also be noted here that the specific yield of the samples (Fig. S3b†) did not dramatically change, showing only a slight increase for the Cu/Fe 0.5 sample, when benchmarking it against the other two samples (Fe and Cu/Fe 0.3).

Apart from the observation of SWCNTs, TEM was also used to observe the catalyst nanoparticles. Remarkably, the analysis revealed an interesting result: the distribution of catalyst nanoparticles remained unchanged despite the addition of copper(II) nitrate trihydrate to the synthesis process (Fig. 5a–c). It can be seen that the mean nanoparticle diameter was about 7.7–8.0 nm for all samples, demonstrating that there is no impact from the addition of copper(II) nitrate trihydrate to the synthesis process. This can be explained by the fact that the chosen heating line temperature of 250 °C is significantly higher than the initial thermal decomposition temperature of the copper precursor, which is around 170–180 °C,[55] and therefore, it is likely that the copper precursor decomposes before reaching the reactor. Instead, the copper oxide formed during decomposition is expected to deposit on the walls of the heating line or at the entrance of the reactor, where temperatures are even higher. Consequently, these oxide nanoparticles do not reach the reactor or participate in the SWCNT synthesis process.

To verify this hypothesis, TEM EDS (Fig. 6) along with SEM EDS mapping (Fig. S4†) and XPS analysis (Fig. S5†) were performed to check for the presence of any traces of copper in the catalyst particles (for all measurements, the Cu/Fe 0.5 sample was selected because it is the one with the highest copper concentration in the solution of precursors). Both SEM EDS mapping and XPS analysis did not show any traces of Cu in the fabricated samples. Fig. 6a shows a representative EDS spectrum of the catalyst nanoparticles and the corresponding TEM micrograph is shown in Fig. 6b. The EDS scan covered the entire image area shown in Fig. 6b, maximizing the inclusion of nanoparticles in a single scan to ensure a comprehensive analysis of their composition. The EDS spectra of the catalyst nanoparticles are shown in Fig. S6.† From these results, it is evident that no copper is present in the composition of the catalyst nanoparticles, confirming the initial assumption that the copper remains in the heating lines of the reactor in the form of copper oxide.

To determine the chirality distribution of the SWCNTs, SAED was employed to analyse the fabricated samples.[56,57]

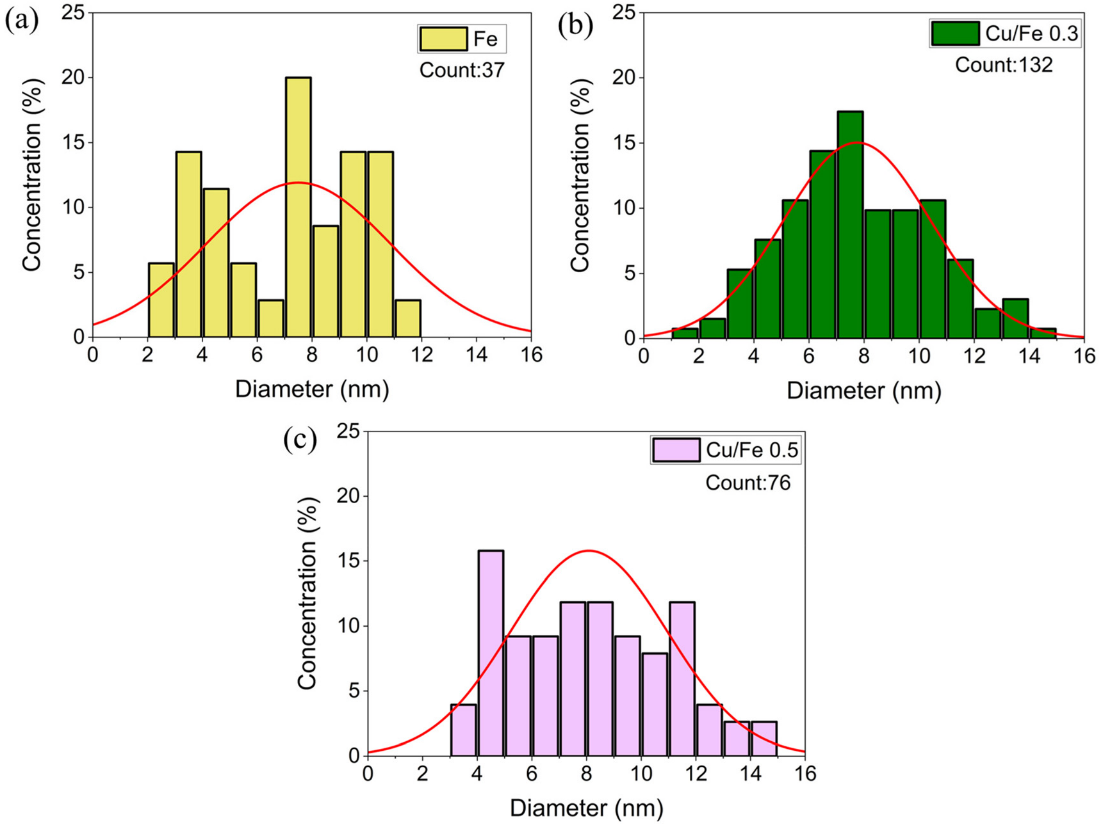

Fig. 5 Nanoparticle diameter distributions of all samples. (a) Fe sample, (b) Cu/Fe 0.3 sample, and (c) Cu/Fe 0.5 sample. The data were analysed from at least 40 individual TEM micrographs for each sample.

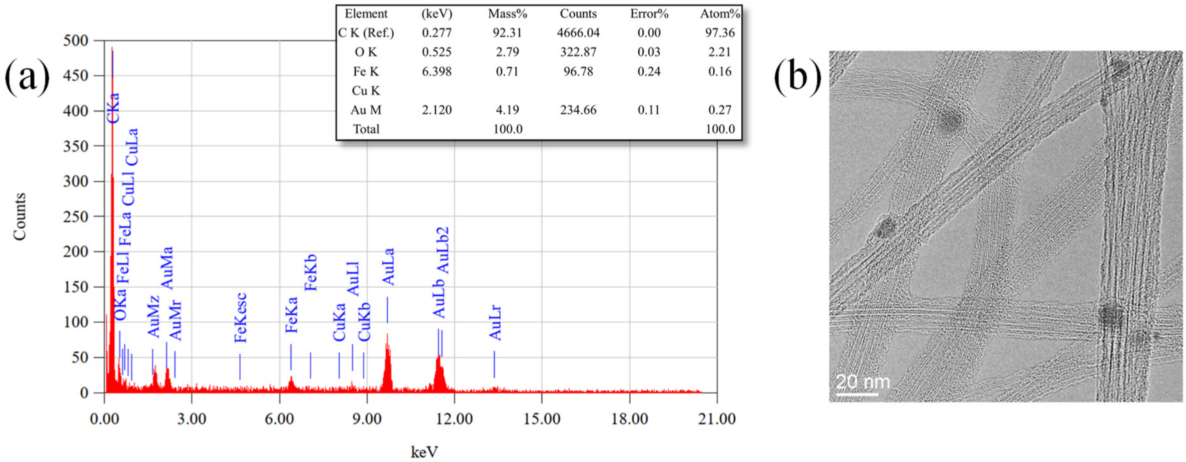

Element	(keV)	Mass%	Counts	Error%	Atom%
C K (Ref.)	0.277	92.31	4666.04	0.00	97.36
O K	0.525	2.79	322.87	0.03	2.21
Fe K	6.398	0.71	96.78	0.24	0.16
Cu K					
Au M	2.120	4.19	234.66	0.11	0.27
Total		100.0			100.0

Fig. 6 EDS analysis of the Cu/Fe 0.5 catalyst nanoparticles. (a) Representative EDS spectrum of the scanned particles and (b) TEM micrograph of the particles in the EDS spectrum.

Fig. 7 illustrates the three chirality distribution maps along with the corresponding diameter and chiral angle distributions derived from the electron diffraction patterns of approximately 140 individual SWCNTs for each sample. It should be noted that well-isolated and separated SWCNTs from nanotube bundles were selected for the analysis. Representative SAED patterns are shown in the ESI (Fig. S7†). Notably, no MWCNTs were observed, either through high-resolution imaging or electron diffraction analysis, and the results are in very good agreement with the light absorption

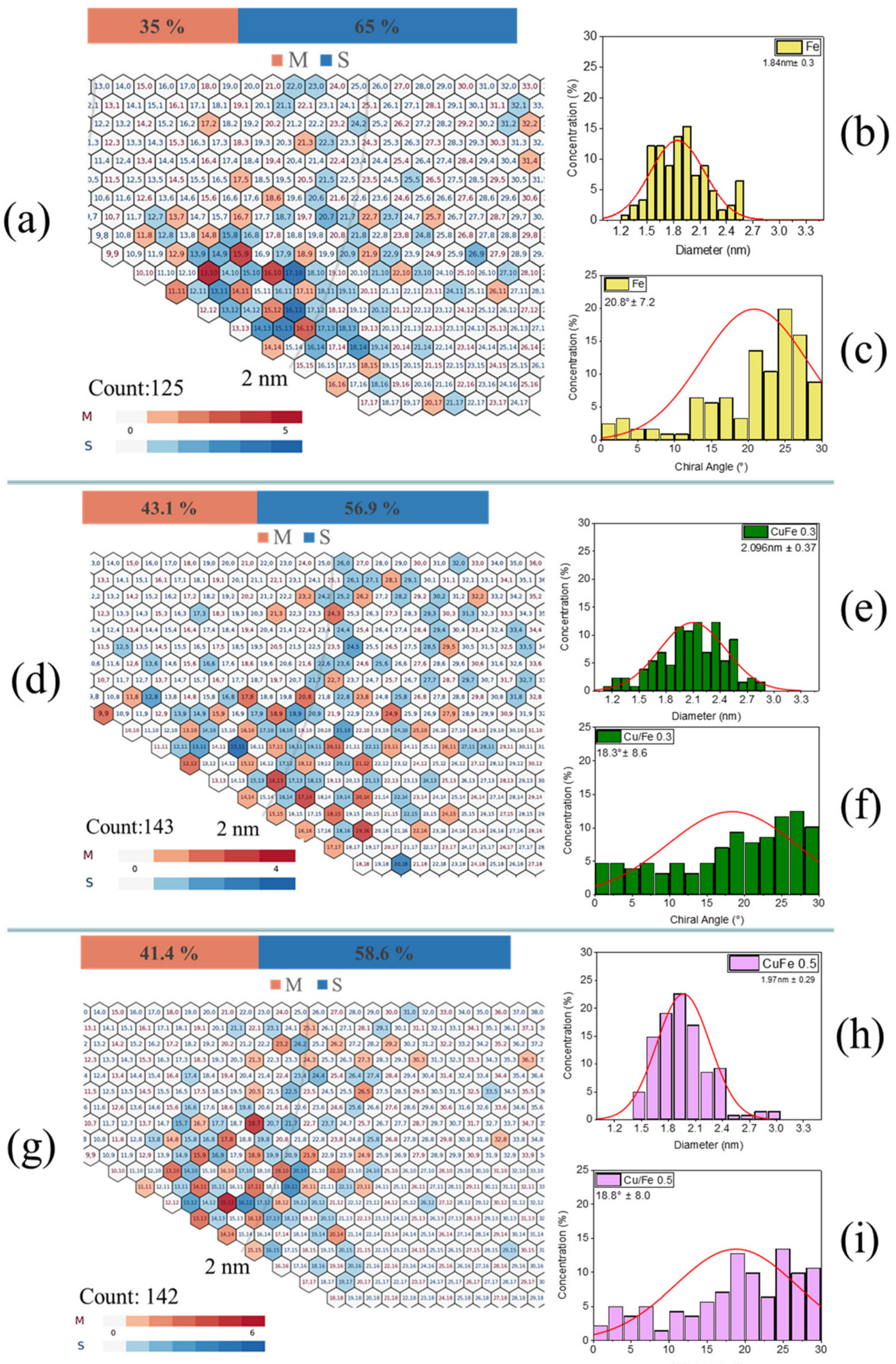

Fig. 7 Chirality maps and the corresponding distributions of diameters and chiral angles for all samples. (a–c) Fe sample, (d–f) Cu/Fe 0.3 sample, and (g–i) Cu/Fe 0.5 sample.

results discussed earlier. The reference Fe sample (Fig. 7a–c) exhibited a near-armchair chirality distribution with a mean chiral angle of 20.80° (Fig. 7c) and a mean diameter of 1.84 nm (Fig. 7b). The percentage of metallic nanotubes was at 35%. On the other hand, the samples with the ferrocenium catalyst exhibited increased percentages of metallic nanotubes, reaching 43.1% for the Cu/Fe 0.3 sample (Fig. 7d–f) and 41.4% for the Cu/Fe 0.5 sample (Fig. 7g–i).

The mean diameters of these samples also increased, reaching 2.10 nm and 1.97 nm, respectively, highlighting the influence of ferrocenium on SWCNT growth. The significant differences in chirality distributions are evident in the chiral angle histograms (Fig. 7f and i), which showed a noticeable decrease in chiral angles from the Fe sample to 18.30° and 18.80°, respectively, indicating a shift in the distribution from a near-armchair region (as seen in the Fe sample) to more scattered distributions with many nanotubes approaching the near-zigzag region. Last but not least, this increase in the mean diameter is in good agreement once more with the UV-vis-NIR results discussed previously.

Previous studies[53] have shown that using ethanol as a carbon source in catalyst-supported CVD methods can lead to the synthesis of near-armchair type SWCNTs with 75–77% being semiconducting, based on TEM SAED. Certain intrinsic properties of ethanol can lead to the preferential growth of near-armchair or semiconducting SWCNTs, where the formation of –OH groups and –H radicals during the initial stage of ethanol decomposition on Fe nanoparticles is thermodynamically and kinetically favourable. These decomposition products, including –OH groups and –H radicals, can selectively etch small-diameter metallic SWCNTs, which have higher curvature energy and lower ionization energy, thereby enriching the fractions of near-armchair or semiconducting SWCNTs. However, our results using a ferrocenium catalyst under the same conditions as ferrocene showed an increase in the amount of metallic SWCNTs, indicating that, in addition to the carbon source and reactor conditions, the choice of catalyst plays a critical role in determining selective chiralities.

3.3 Suggested SWCNT chirality change mechanism

One critical parameter that can affect the chirality of grown nanotubes is the charge of the catalyst nanoparticles. In our study, we explored the effect of ferrocene and ferrocenium catalysts on the chirality of SWCNTs, where the key difference between these catalysts lies in their charge: Fe^{2+} is less positively charged, while Fe^{3+} carries a higher positive charge.

This charge difference significantly alters the ability of the catalyst to facilitate helicity transitions in growing SWCNTs.[58] When the catalyst is in the Fe^{3+} state, its higher positive charge leads to a stronger electrostatic potential, which increases the re-nucleation barrier at the nanotube–catalyst interface. As a result, the nanotube structure remains largely fixed, making helicity transitions highly improbable. In contrast, Fe^{2+} has a lower positive charge and can acquire more negative charge during growth, leading to a reduction in the re-nucleation barrier. This lower barrier allows the occurrence of structural rearrangements at the nanotube–catalyst interface, making helicity transitions more likely. Specifically, the reduced re-nucleation barrier favours a transition from the metallic to semiconducting state in SWCNTs (Fig. 8a). This effect aligns with the induced charge mechanism, where a more negatively charged catalyst raises the Fermi level, shifting the electronic density of states (DOS) and making semiconducting SWCNTs more stable. As a result, the Fe^{2+} catalyst, with its ability to lower the re-nucleation barriers more effectively, plays a crucial role in facilitating the helicity change, whereas Fe^{3+} is less effective in this regard.

To justify the proposed mechanism, we investigated the average net charge of the produced nanotubes and catalyst particles using an aerosol electrometer 3068B instrument. The results of the net charge measurements are shown in Fig. 8b. The data in Fig. 8b show that the Cu/Fe 0.3 and Cu/Fe 0.5 samples possessed more positive net charge than the ferrocene samples (−71 fA and −64 fA *vs.* −103 fA), which is in good agreement with the proposed mechanism above. These experimental data strengthen the conclusion that Fe^{2+} is more effective in inducing helicity changes, where Fe^{3+} could retain the initial chirality of grown SWCNTs. It should be noted here that previous FC-CVD works investigated the effect of net charge on SWCNT synthesis and found that more negative net charge was associated with the existence of more s-SWCNTs in the fabricated films, which is in good agreement with our results as well.[59] Based on the diameter analysis from TEM

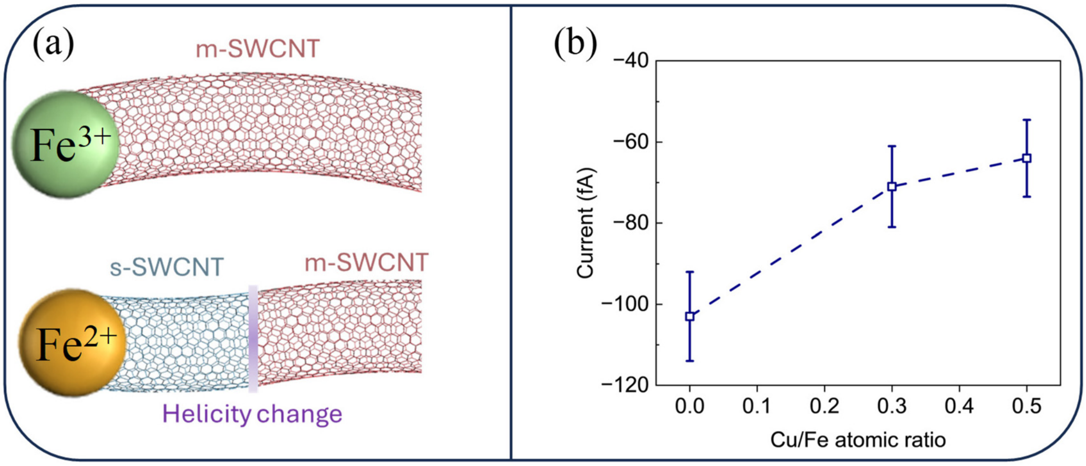

Fig. 8 (a) Proposed mechanism for the chirality changes of SWCNTs using ferrocene and ferrocenium catalysts and (b) aerosol electrometer measurements of all samples.

(Fig. 7b, e and h) and the observed increase in SWCNT diameter from 1.84 nm to 2.10 nm, it can be assumed that the Cu/Fe samples initially contained a higher proportion of smaller-diameter metallic nanotubes, which were likely etched away by exposure to H_2 or by-products of ethanol decomposition, such as CO_2 or H_2O.[32] This etching process selectively removed the smaller metallic nanotubes, resulting in a shift in the overall diameter distribution towards larger diameters and, consequently, the statistical analysis showed different diameter distributions, reflecting this etching effect.

4. Conclusion

This study demonstrates the significant influence of ferrocenium on the chirality of SWCNTs synthesized using the FC-CVD method. By introducing ferrocenium into the catalyst system, we observed a substantial enhancement in the metallicity of the grown nanotubes, increasing the proportion of metallic SWCNTs to 43.1%, the diameter distribution of the nanotubes from 1.84 nm to 2.10 nm, and the bundle diameter from 11.20 nm to 18.40 nm. The key factor behind this metallicity enhancement is the positive charge of the Fe^{3+} in ferrocenium, which positions the Fermi level in a way that stabilizes the formation of metallic nanotubes without significantly lowering the re-nucleation barrier for helicity changes. Nevertheless, this positively charged catalyst alters the growth dynamics, promoting the formation of metallic nanotubes over semiconducting ones. These findings underscore the crucial role of catalyst charge in determining the chirality and electronic properties of SWCNTs. The ability of Fe^{3+} in ferrocenium to enhance the metallicity of SWCNTs opens up new possibilities for tailoring nanotube synthesis towards the desired electronic characteristics, offering valuable insights into future applications in nanoelectronics and materials science.

Author contributions

Anastasios Karakassides: conceptualization, writing – original draft, methodology, investigation, data curation, and validation. Hirotaka Inoue: writing – review & editing. Peng Liu: writing – review & editing. Zhenyu Xu: writing – review & editing. Ghulam Yasin: writing – review & editing. Hua Jiang: methodology and writing – review & editing. Esko I. Kauppinen: conceptualization, writing – review & editing, supervision, funding acquisition, and resources.

Data availability

The data supporting this article have been included as part of the ESI.†

Conflicts of interest

The authors declare that they have no known competing financial interests or personal relationships that could have appeared to influence the work reported in this paper.

Acknowledgements

The authors are grateful to Aalto University and the Department of Applied Physics for their facilities and technical support at the OtaNano-NanoMicroscopy Center (Aalto-NMC). The authors are also grateful to Dr Jani Sainio for acquiring XPS spectra of the SWCNT films.

References

1 S. Paul and D.-W. Kim, Preparation and Characterization of Highly Conductive Transparent Films with Single-Walled Carbon Nanotubes for Flexible Display Applications, *Carbon*, 2009, **47**(10), 2436–2441.

2 S. Kumar, M. Nehra, D. Kedia, N. Dilbaghi, K. Tankeshwar and K.-H. Kim, Carbon Nanotubes: A Potential Material for Energy Conversion and Storage, *Prog. Energy Combust. Sci.*, 2018, **64**, 219–253.

3 A. A. Bhirde, S. Patel, A. A. Sousa, V. Patel, A. A. Molinolo, Y. Ji, R. D. Leapman, J. S. Gutkind and J. F. Rusling, Distribution and Clearance of PEG-Single-Walled Carbon Nanotube Cancer Drug Delivery Vehicles in Mice, *Nanomedicine*, 2010, **5**(10), 1535–1546.

4 M. T. Hasan, E. Campbell, O. Sizova, V. Lyle, G. Akkaraju, D. L. Kirkpatrick and A. V. Naumov, Multi-Drug/Gene NASH Therapy Delivery and Selective Hyperspectral NIR Imaging Using Chirality-Sorted Single-Walled Carbon Nanotubes, *Cancers*, 2019, **11**(8), 1175.

5 K. M. Lee, C. P. P. Wong, T. L. Tan and C. W. Lai, Functionalized Carbon Nanotubes for Adsorptive Removal of Water Pollutants, *Mater. Sci. Eng., B*, 2018, **236–237**, 61–69.

6 T. Rasheed, M. Adeel, F. Nabeel, M. Bilal and H. M. N. Iqbal, TiO_2/SiO_2 Decorated Carbon Nanostructured Materials as a Multifunctional Platform for Emerging Pollutants Removal, *Sci. Total Environ.*, 2019, **688**, 299–311.

7 M. S. Dresselhaus, G. Dresselhaus and R. Saito, Physics of Carbon Nanotubes, *Carbon*, 1995, **33**(7), 883–891.

8 H. E. Unalan, G. Fanchini, A. Kanwal, A. Du Pasquier and M. Chhowalla, Design Criteria for Transparent Single-Wall Carbon Nanotube Thin-Film Transistors, *Nano Lett.*, 2006, **6**(4), 677–682.

9 A. Pasquier, H. E. Du Unalan, A. Kanwal, S. Miller and M. Chhowalla, Conducting and Transparent Single-Wall Carbon Nanotube Electrodes for Polymer-Fullerene Solar Cells, *Appl. Phys. Lett.*, 2005, **87**(20), 203511.

10 X. Cao, H. Chen, X. Gu, B. Liu, W. Wang, Y. Cao, F. Wu and C. Zhou, Screen Printing as a Scalable and Low-Cost Approach for Rigid and Flexible Thin-Film Transistors Using Separated Carbon Nanotubes, *ACS Nano*, 2014, **8**(12), 12769–12776.

11 A. Maffucci, G. Miano and F. Villone, A Transmission Line Model for Metallic Carbon Nanotube Interconnects, *Int. J. Circuit Theory Appl.*, 2008, **36**(1), 31–51.

12 C. Villeneuve, S. Pacchini, P. Boulanger, A. Brouzes, F. Roussel, M. Pinault, M. Mayne-L'Hermite and R. Plana, Local Current Mapping of Single Vertically Aligned Multi-Walled Carbon Nanotube in a Polymer Matrix, *J. Appl. Phys.*, 2012, **112**(8), 084327.

13 A. Takakura, K. Beppu, T. Nishihara, A. Fukui, T. Kozeki, T. Namazu, Y. Miyauchi and K. Itami, Strength of Carbon Nanotubes Depends on Their Chemical Structures, *Nat. Commun.*, 2019, **10**, 3040.

14 Z. Zhu, N. Wei, W. Cheng, B. Shen, S. Sun, J. Gao, Q. Wen, R. Zhang, J. Xu, Y. Wang and F. Wei, Rate-Selected Growth of Ultrapure Semiconducting Carbon Nanotube Arrays, *Nat. Commun.*, 2019, **10**, 4467.

15 X. Li, F. Zhang, L. Zhang, Z.-H. Ji, Y.-M. Zhao, Z.-W. Xu, Y. Wang, P.-X. Hou, M. Tian, H.-B. Zhao, S. Jiang, L.-Q. Ping, H.-M. Cheng and C. Liu, Kinetics-Controlled Growth of Metallic Single-Wall Carbon Nanotubes from $CoRe_x$ Nanoparticles, *ACS Nano*, 2022, **16**(1), 232–240.

16 M. He, H. Jiang, J. Lehtonen and E. I. Kauppinen, Growth of Single-Walled Carbon Nanotubes with Large Chiral Angles on Rhodium Nanoparticles, *Nanoscale*, 2013, **5**(21), 10200.

17 F. Yang, X. Wang, D. Zhang, K. Qi, J. Yang, Z. Xu, M. Li, X. Zhao, X. Bai and Y. Li, Growing Zigzag (16,0) Carbon Nanotubes with Structure-Defined Catalysts, *J. Am. Chem. Soc.*, 2015, **137**(27), 8688–8691.

18 F. Yang, X. Wang, J. Si, X. Zhao, K. Qi, C. Jin, Z. Zhang, M. Li, D. Zhang, J. Yang, Z. Zhang, Z. Xu, L.-M. Peng, X. Bai and Y. Li, Water-Assisted Preparation of High-Purity Semiconducting (14,4) Carbon Nanotubes, *ACS Nano*, 2017, **11**(1), 186–193.

19 S. Zhang, L. Kang, X. Wang, L. Tong, L. Yang, Z. Wang, K. Qi, S. Deng, Q. Li, X. Bai, F. Ding and J. Zhang, Arrays of Horizontal Carbon Nanotubes of Controlled Chirality Grown Using Designed Catalysts, *Nature*, 2017, **543**(7644), 234–238.

20 L. Kang, S. Deng, S. Zhang, Q. Li and J. Zhang, Selective Growth of Subnanometer Diameter Single-Walled Carbon Nanotube Arrays in Hydrogen-Free CVD, *J. Am. Chem. Soc.*, 2016, **138**(39), 12723–12726.

21 F. Ding, A. R. Harutyunyan and B. I. Yakobson, Dislocation Theory of Chirality-Controlled Nanotube Growth, *Proc. Natl. Acad. Sci.U. S. A.*, 2009, **106**((8)), 2506–2509.

22 F. Zhang, L. Zhang, H. Jiang, X. Li, F. Liu, Z.-H. Ji, P.-X. Hou, S. Guo, H.-M. Cheng, E. I. Kauppinen, C. Liu and F. Ding, Growth of High-Density Single-Wall Carbon Nanotubes with a Uniform Structure Using a CoRu Catalyst, *Carbon*, 2023, **209**, 118011.

23 F. Yang, X. Wang, D. Zhang, J. Yang, D. Luo, Z. Xu, J. Wei, J. Q. Wang, Z. Xu, F. Peng, X. Li, R. Li, Y. Li, M. Li, X. Bai, F. Ding and Y. Li, Chirality-Specific Growth of Single-Walled Carbon Nanotubes on Solid Alloy Catalysts, *Nature*, 2014, **510**(7506), 522–524.

24 C. A. Eveleens, Y. Hijikata, S. Irle and A. J. Page, Chiral-Selective Carbon Nanotube Etching with Ammonia: A Quantum Chemical Investigation, *J. Phys. Chem. C*, 2016, **120**(35), 19862–19870.

25 W. S. Li, P. X. Hou, C. Liu, D. M. Sun, J. Yuan, S. Y. Zhao, L. C. Yin, H. Cong and H. M. Cheng, High-Quality, Highly Concentrated Semiconducting Single-Wall Carbon Nanotubes for Use in Field Effect Transistors and Biosensors, *ACS Nano*, 2013, **7**(8), 6831–6839.

26 C. M. Yang, J. S. Park, K. H. An, S. C. Lim, K. Seo, B. Kim, K. A. Park, S. Han, C. Y. Park and Y. H. Lee, Selective Removal of Metallic Single-Walled Carbon Nanotubes with Small Diameters by Using Nitric and Sulfuric Acids, *J. Phys. Chem. B*, 2005, **109**(41), 19242–19248.

27 X. Q. Li, P. X. Hou, C. Liu and H. M. Cheng, Preparation of Metallic Single-Wall Carbon Nanotubes, *Carbon*, 2019, **147**, 187–198.

28 W. J. Yu, S. H. Chae, Q. A. Vu and Y. H. Lee, Sorting Centimetre-Long Single-Walled Carbon Nanotubes, *Sci. Rep.*, 2016, **6**, 30836.

29 M. He, X. Wang, S. Zhang, H. Jiang, F. Cavalca, H. Cui, J. B. Wagner, T. W. Hansen, E. Kauppinen, J. Zhang and F. Ding, Growth Kinetics of Single-Walled Carbon Nanotubes with a (2n, n) Chirality Selection, *Sci. Adv.*, 2019, **5**(12), eaav9668.

30 C. Liu and H. M. Cheng, Controlled Growth of Semiconducting and Metallic Single-Wall Carbon Nanotubes, *J. Am. Chem. Soc.*, 2016, **138**(21), 6690–6698.

31 M. D. Yadav, A. W. Patwardhan, J. B. Joshi and K. Dasgupta, Selective Synthesis of Metallic and Semi-Conducting Single-Walled Carbon Nanotube by Floating Catalyst Chemical Vapour Deposition, *Diamond Relat. Mater.*, 2019, **97**, 107432.

32 P. Liu, A. T. Khan, E. X. Ding, Q. Zhang, Z. Xu, X. Bai, N. Wei, Y. Tian, D. Li, H. Jiang, H. Lipsanen, Z. Sun and E. I. Kauppinen, Direct Synthesis of Semiconducting Single-Walled Carbon Nanotubes Toward High-Performance Electronics, *Adv. Electron. Mater.*, 2023, **9**(7), 2300196.

33 Y. Liao, H. Jiang, N. Wei, P. Laiho, Q. Zhang, S. A. Khan and E. I. Kauppinen, Direct Synthesis of Colorful Single-Walled Carbon Nanotube Thin Films, *J. Am. Chem. Soc.*, 2018, **140**(31), 9797–9800.

34 Q. Yu, C. Wu and L. Guan, Direct Enrichment of Metallic Single-Walled Carbon Nanotubes by Using NO2 as Oxidant to Selectively Etch Semiconducting Counterparts, *J. Phys. Chem. Lett.*, 2016, **7**(22), 4470–4474.

35 S. Y. Moon, S. Y. Jeon, S. H. Lee, A. Lee and S. M. Kim, High Purity Single Wall Carbon Nanotube by Oxygen-Containing Functional Group of Ferrocene-Derived Catalyst

Precursor by Floating Catalyst Chemical Vapor Deposition, *Nanomaterials*, 2022, **12**(5), 863.

36 M. Cuartero, L. Chai, B. Zhang, R. De Marco and G. A. Crespo, Ferrocene Self Assembled Monolayer as a Redox Mediator for Triggering Ion Transfer across Nanometer-Sized Membranes, *Electrochim. Acta*, 2019, **315**, 84–93.

37 S. Mathi, P. K. Gupta, R. Kumar, R. K. Nagarale and A. Sharma, Ferrocenium Ion Confinement in Polyelectrolyte for Electrochemical Nitric Oxide Sensor, *ChemistrySelect*, 2019, **4**(13), 3833–3840.

38 L. Fabbrizzi, The Ferrocenium/Ferrocene Couple: A Versatile Redox Switch, *ChemTexts*, 2020, **6**, 22.

39 X. Liu, Y. Luo, Y. Chen, S. Wu and Z. Li, From Glow to Growth: Chemiluminescence Induced Cationic Polymerization Using Ferrocenium Salt, *Macromol. Chem. Phys.*, 2023, **224**(13), 2300048.

40 X. Meng, H. Lu, Z. Li, C. Wang, R. Liu, X. Guan and Y. Yagci, Near-Infrared Light Induced Cationic Polymerization Based on Upconversion and Ferrocenium Photochemistry, *Polym. Chem.*, 2019, **10**(41), 5574–5577.

41 Q. Wu, Z. Ji, L. Xin, D. Li, L. Zhang, C. Liu, T. Yang, Z. Wen, H. Wang, B. Xin, H. Xue, F. Chen, Z. Xu, H. Cui and M. He, Iron Silicide-Catalyzed Growth of Single-Walled Carbon Nanotubes with a Narrow Diameter Distribution, *Carbon*, 2019, **149**, 139–143.

42 Y. Tian, H. Jiang, P. Laiho and E. I. Kauppinen, Validity of Measuring Metallic and Semiconducting Single-Walled Carbon Nanotube Fractions by Quantitative Raman Spectroscopy, *Anal. Chem.*, 2018, **90**(4), 2517–2525.

43 A. Castan, S. Forel, F. Fossard, J. Defillet, A. Ghedjatti, D. Levshov, W. Wenseleers, S. Cambré and A. Loiseau, Assessing the Reliability of the Raman Peak Counting Method for the Characterization of SWCNT Diameter Distributions: A Cross Characterization with TEM, *Carbon*, 2021, **171**, 968–979.

44 Y. Tian, H. Jiang, J. V. Pfaler, Z. Zhu, A. G. Nasibulin, T. Nikitin, B. Aitchison, L. Khriachtchev, D. P. Brown and E. I. Kauppinen, Analysis of the Size Distribution of Single-Walled Carbon Nanotubes Using Optical Absorption Spectroscopy, *J. Phys. Chem. Lett.*, 2010, **1**((7)), 1143–1148.

45 E. X. Ding, A. Hussain, S. Ahmad, Q. Zhang, Y. Liao, H. Jiang and E. I. Kauppinen, High-Performance Transparent Conducting Films of Long Single-Walled Carbon Nanotubes Synthesized from Toluene Alone, *Nano Res.*, 2020, **13**(1), 112–120.

46 Š. Toma and R. Šebesta, Applications of Ferrocenium Salts in Organic Synthesis, *Synthesis*, 2015, (12), 1683–1695.

47 J. Irangu and R. B. Jordan, Oxidation of Ferrocenes by Copper(II) in Aqueous Acetonitrile: Nitrate and Chloride Ion Effects, *Inorg. Chem.*, 2007, **46**(4), 1451–1458.

48 C. Swearingen, J. Wu, J. Stucki and A. Fitch, Use of Ferrocenyl Surfactants of Varying Chain Lengths to Study Electron Transfer Reactions in Native Montmorillonite Clay, *Environ. Sci. Technol.*, 2004, **38**(21), 5598–5603.

49 T. Akitsu, J. Yamaguchi, N. Uchida and Y. Aritake, The Studies of Conditions for Inducing Chirality to Cu(II) Complexes by Chiral Zn(II) and Ni(II) Complexes with Schiff Base, *Res. Lett. Mater. Sci.*, 2009, **2009**, 484172.

50 E. X. Ding, Q. Zhang, N. Wei, A. T. Khan and E. I. Kauppinen, High-Performance Single-Walled Carbon Nanotube Transparent Conducting Film Fabricated by Using Low Feeding Rate of Ethanol Solution, *R. Soc. Open Sci.*, 2018, **5**(6), 180392.

51 A. Jorio and R. Saito, Raman Spectroscopy for Carbon Nanotube Applications, *J. Appl. Phys.*, 2021, **129**(2), 21102.

52 Y. Miyata, K. Yanagi, Y. Maniwa and H. Kataura, Optical Evaluation of the Metal-to-Semiconductor Ratio of Single-Wall Carbon Nanotubes, *J. Phys. Chem. C*, 2008, **112**(34), 13187–13191.

53 E.-X. Ding, H. Jiang, Q. Zhang, Y. Tian, P. Laiho, A. Hussain, Y. Liao, N. Wei and E. I. Kauppinen, Highly Conductive and Transparent Single-Walled Carbon Nanotube Thin Films from Ethanol by Floating Catalyst Chemical Vapor Deposition, *Nanoscale*, 2017, **9**(44), 17601–17609.

54 Q. Zhang, J. S. Nam, J. Han, S. Datta, N. Wei, E. X. Ding, A. Hussain, S. Ahmad, V. Skakalova, A. T. Khan, Y. P. Liao, M. Tavakkoli, B. Peng, K. Mustonen, D. Kim, I. Chung, S. Maruyama, H. Jiang, I. Jeon and E. I. Kauppinen, Large-Diameter Carbon Nanotube Transparent Conductor Overcoming Performance–Yield Tradeoff, *Adv. Funct. Mater.*, 2022, **32**(11), 2103397.

55 P. Wiecinski and A. Wieclaw-Midor, Metal Salts as Dopants for ZnO Ceramics-Thermogravimetry Coupled with Mass Spectrometry Studies, *J. Therm. Anal. Calorim.*, 2022, **147**(10), 5599–5615.

56 H. Jiang, A. G. Nasibulin, D. P. Brown and E. I. Kauppinen, Unambiguous Atomic Structural Determination of Single-Walled Carbon Nanotubes by Electron Diffraction, *Carbon*, 2007, **45**(3), 662–667.

57 H. Jiang, D. P. Brown, A. G. Nasibulin and E. I. Kauppinen, Robust Bessel-Function-Based Method for Determination of the (n, m) Indices of Single-Walled Carbon Nanotubes by Electron Diffraction, *Phys. Rev. B:Condens. Matter Mater. Phys.*, 2006, **74**(3), 035427.

58 J. Wang, X. Jin, Z. Liu, G. Yu, Q. Ji, H. Wei, J. Zhang, K. Zhang, D. Li, Z. Yuan, J. Li, P. Liu, Y. Wu, Y. Wei, J. Wang, Q. Li, L. Zhang, J. Kong, S. Fan and K. Jiang, Growing Highly Pure Semiconducting Carbon Nanotubes by Electrotwisting the Helicity, *Nat. Catal.*, 2018, **1**(5), 326–331.

59 E.-X. Ding, P. Liu, A. T. Khan, Q. Zhang, N. Wei, H. Jiang and E. I. Kauppinen, Towards the Synthesis of Semiconducting Single-Walled Carbon Nanotubes by Floating-Catalyst Chemical Vapor Deposition: Challenges of Reproducibility, *Carbon*, 2022, **195**, 92–100.